Synthetic and Systems Biotechnology 7 (2022) 738–749

Contents lists available at ScienceDirect

Synthetic and Systems Biotechnology

journal homepage: www.keaipublishing.com/en/journals/synthetic-and-systems-biotechnology

Original Research Article

Comparative functional genomics identifies an iron-limited bottleneck in a *Saccharomyces cerevisiae* strain with a cytosolic-localized isobutanol pathway

Francesca V. Gambacorta [a,b], Ellen R. Wagner [a,c,1], Tyler B. Jacobson [a,d,1], Mary Tremaine [a], Laura K. Muehlbauer [e], Mick A. McGee [a], Justin J. Baerwald [b], Russell L. Wrobel [a,c,f], John F. Wolters [a,c,f], Mike Place [a], Joshua J. Dietrich [a,b], Dan Xie [a], Jose Serate [a], Shabda Gajbhiye [a], Lisa Liu [a,d], Maikayeng Vang-Smith [a], Joshua J. Coon [e,g], Yaoping Zhang [a], Audrey P. Gasch [a,c], Daniel Amador-Noguez [a,d], Chris Todd Hittinger [a,c,f], Trey K. Sato [a], Brian F. Pfleger [a,b,*]

[a] DOE Great Lakes Bioenergy Research Center, University of Wisconsin-Madison, Madison, WI, USA
[b] Department of Chemical and Biological Engineering, University of Wisconsin-Madison, Madison, WI, USA
[c] Laboratory of Genetics, Center for Genomic Science Innovation, University of Wisconsin-Madison, Madison, WI, USA
[d] Department of Bacteriology, University of Wisconsin-Madison, Madison, WI, USA
[e] Department of Chemistry, University of Wisconsin-Madison, Madison, WI, USA
[f] Wisconsin Energy Institute, J. F. Crow Institute for the Study of Evolution, University of Wisconsin-Madison, Madison, WI, USA
[g] Department of Biomolecular Chemistry, University of Wisconsin-Madison, Madison, WI, USA

ARTICLE INFO

Keywords:
Saccharomyces cerevisiae
Isobutanol
Functional genomics analysis
Pathway localization
Fe incorporation

ABSTRACT

Metabolic engineering strategies have been successfully implemented to improve the production of isobutanol, a next-generation biofuel, in *Saccharomyces cerevisiae*. Here, we explore how two of these strategies, pathway re-localization and redox cofactor-balancing, affect the performance and physiology of isobutanol producing strains. We equipped yeast with isobutanol cassettes which had either a mitochondrial or cytosolic localized isobutanol pathway and used either a redox-imbalanced (NADPH-dependent) or redox-balanced (NADH-dependent) ketol-acid reductoisomerase enzyme. We then conducted transcriptomic, proteomic and metabolomic analyses to elucidate molecular differences between the engineered strains. Pathway localization had a large effect on isobutanol production with the strain expressing the mitochondrial-localized enzymes producing 3.8-fold more isobutanol than strains expressing the cytosolic enzymes. Cofactor-balancing did not improve isobutanol titers and instead the strain with the redox-imbalanced pathway produced 1.5-fold more isobutanol than the balanced version, albeit at low overall pathway flux. Functional genomic analyses suggested that the poor performances of the cytosolic pathway strains were in part due to a shortage in cytosolic Fe–S clusters, which are required cofactors for the dihydroxyacid dehydratase enzyme. We then demonstrated that this cofactor limitation may be partially recovered by disrupting iron homeostasis with a *fra2* mutation, thereby increasing cellular iron levels. The resulting isobutanol titer of the *fra2* null strain harboring a cytosolic-localized isobutanol pathway outperformed the strain with the mitochondrial-localized pathway by 1.3-fold, demonstrating that both localizations can support flux to isobutanol.

Peer review under responsibility of KeAi Communications Co., Ltd.
* Corresponding author. 3629 Engineering Hall, 1415 Engineering Drive, Madison, WI, 53706, United States.
E-mail address: pfleger@engr.wisc.edu (B.F. Pfleger).
[1] these authors contributed equally to this manuscript.

https://doi.org/10.1016/j.synbio.2022.02.007
Received 26 October 2021; Received in revised form 17 December 2021; Accepted 14 February 2022

1. Introduction

Isobutanol is a branched four-carbon alcohol targeted by many as a biofuel for light-duty engines and as a precursor to jet and diesel fuels via catalytic upgrading [1]. Relative to ethanol, isobutanol has a higher energy density, a lower vapor pressure, and a higher flash point, making it a better option for spark-ignition engines. Isobutanol is also less corrosive and less hygroscopic, making it a better biofuel for current piping infrastructure [2]. Isobutanol biosynthesis is redox balanced with glycolysis and can therefore be made via fermentation. *Saccharomyces cerevisiae*, the workhorse for industrial fermentations, is therefore a suitable host for its production. While yeast have a natural ability to synthesize isobutanol, there are many barriers to making isobutanol the primary fermentation product at high rates [3].

S. cerevisiae synthesizes isobutanol from pyruvate via enzymes involved in valine biosynthesis and the Ehrlich pathway. The first half of the pathway converts pyruvate to α-ketoisovalerate (KIV) by mitochondria-localized *ILV* enzymes: acetolactate synthase (ALS, encoded by *ILV2*), a NADPH-dependent ketol-acid reductoisomerase (KARI, encoded by *ILV5*), and a 2Fe–2S cluster-requiring dihydroxyacid dehydratase (DHAD, encoded by *ILV3*). The second part of the pathway, the Ehrlich pathway, converts KIV to isobutanol by promiscuous cytosolic enzymes: α-ketoacid decarboxylase (KDC, encoded by pyruvate decarboxylases, *PDC1 PDC5 or PDC6*, or phenylpyruvate decarboxylase, *ARO10*) and a NADH-dependent alcohol dehydrogenase (ADH, encoded by *ADH1-5*) (Fig. 1a). *S. cerevisiae's* native isobutanol production is low (<1% of the theoretical maximum yield), so substantial work is needed to make isobutanol the primary fermentation product [4–6].

The spatial segregation of the native pathway enzymes, split between the mitochondria and the cytosol, may be a limiting factor for synthesizing isobutanol at high levels. The segregation can be overcome by localizing the five-step pathway into a single compartment: mitochondrial localization is achieved by adding a mitochondrial localization sequence (MLS) to the genes in the Ehrlich pathway (*PDC1/5/6* or *ARO10* and *ADH1-5*), and cytosolic localization is achieved by removing the MLS sequence from the genes in the valine biosynthesis pathway (*ILV2*, *ILV5*, and *ILV3*) [5,6]. However, the role that localization plays in isobutanol production is obscured by conflicting reports in the literature as both pathway localizations have achieved similar isobutanol titers and yields (Table 1). It has been shown that a strain with mitochondrial-localization benefits from having a higher local concentration of enzyme and pathway intermediates [5]. On the other hand, it has been proposed that cytosolic localization would be preferable in the context of industrially relevant conditions such as high glucose concentrations or anaerobic growth. This is in part because the mitochondria are known to enter a minimal energy-requirement mode under those conditions [7,8].

A second limitation in the isobutanol pathway is the redox cofactor-imbalance that exists between glycolysis and isobutanol fermentation; glycolysis produces two NADH per molecule of glucose, while isobutanol fermentation consumes one NADPH by *ILV5* and one NADH by *ADH*. This results in an NADPH shortage and NADH excess. One strategy to resolve this imbalance is to use a heterologous NADH-dependent KARI, such as the *E. coli* KARI variant, *ilvC*^{6E6}, that was previously engineered with improved specificity towards NADH [9,10]. Another strategy is to increase the supply of NADPH by introducing a transhydrogenase-like shunt ($NADH + NADP^+ \rightarrow NAD^+ + NADPH$) into *S. cerevisiae* [11]. Both strategies have been successful in improving

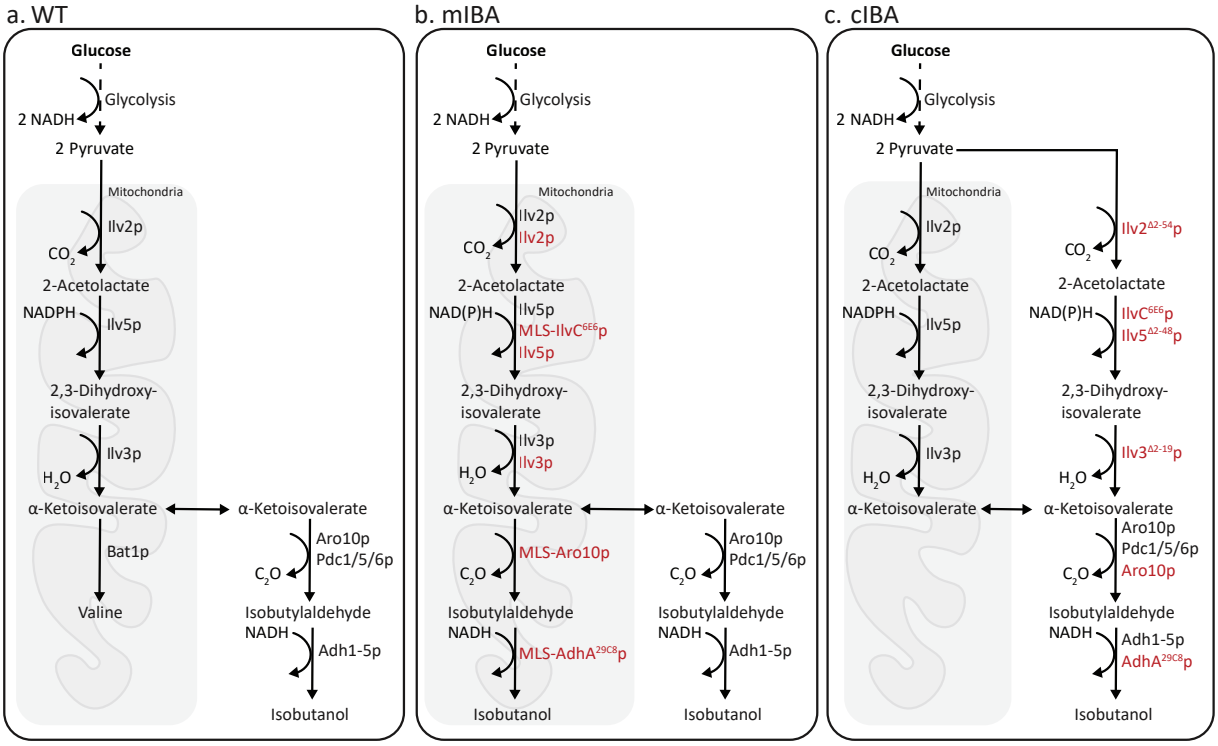

Fig. 1. Native and engineered *S. cerevisiae* isobutanol pathways. a) Shows the endogenous isobutanol synthesis pathway from pyruvate. The first half of the pathway converts pyruvate to α-ketoisovalerate (KIV) by the mitochondrial-localized valine biosynthesis enzymes Ilv2p, Ilv5p, and Ilv3p. The second part of the pathway, the Ehrlich pathway, converts KIV to isobutanol by promiscuous cytosolic-localized decarboxylase enzymes Pdc1/5/6p or Aro10p and Adh1-5p. **b)** Mitochondrial-localized isobutanol pathway (mIBA) consists of codon-optimized variants of *S. cerevisiae* Ilv2p, *S. cerevisiae* Ilv3p, mitochondrial targeted *S. cerevisiae* Aro10p, mitochondrial targeted *L. lactis* AdhA^{29C8}p, and either *S. cerevisiae* Ilv5p or mitochondrial targeted *E. coli* IlvC^{6E6}p for the redox cofactor imbalanced and balanced pathways respectively (red enzymes). **c)** Cytosolic-localized isobutanol pathway (cIBA) consists of codon-optimized variants of *S. cerevisiae* Ilv2$^{\Delta 2\text{-}54}$p, *S. cerevisiae* Ilv3$^{\Delta 2\text{-}19}$p, *S. cerevisiae* Aro10p, *L. lactis* AdhA^{29C8}p, and either *S. cerevisiae* Ilv5$^{\Delta 2\text{-}48}$p or *E. coli* IlvC^{6E6}p for the redox cofactor imbalanced and balanced pathways respectively (red enzymes). For both the mIBA and cIBA pathways, the endogenous/native enzymes (Ilv2p, Ilv5p, Ilv3p, Aro10p, Pdc1/5/6p, Adh1-5p, and Bat1p) in black remain in each strain. (For interpretation of the references to colour in this figure legend, the reader is referred to the Web version of this article.)

Table 1
Highlight report of engineered *S. cerevisiae* strains for isobutanol production.

Pathway localization	NAD^+ regeneration	Overexpress isobutanol genes	Block competing pathway	Metabolic control of ethanol production	Isobutanol titer (mg/L)	Isobutanol yield (mg/g carbon source)	Conditions (carbon source, condition, vessel)	Refs	Year
Mito		✓			635±23	6.4±0.2	Glucose, semi-aerobic, batch	[5]	2013
Cyto		✓	✓		630.27±14.18	14.86±0.55	Glucose, aerobic, batch	[6]	2012
Cyto and mito	✓	✓	✓		1620±110	16.0±1.0	Glucose, semi-aerobic, batch	[11]	2013
Mito		✓	✓		1245±33	12.45	Glucose, aerobic, batch	[12]	2017
Cyto and mito	✓	✓	✓		224±5	12.04±0.23	Glucose, semi-aerobic, batch	[13]	2015
Cyto and mito		✓	✓		330.9	16.55	Glucose, aerobic, batch	[14]	2016
Cyto		✓	✓		2090	59.55	Glucose, aerobic, batch	[4]	2019
Cyto		✓	✓		263.2	13.16	Glucose, semi-aerobic, batch	[15]	2019
Mito		✓	✓	✓	8494.6±305.3	53.5±8.4	Glucose, micro-aerobic, batch and fed-batch	[16]	2018
Cyto	✓	✓	✓		148±24	7.4± 1.2	Glucose, micro-aerobic, batch	[9]	2016
Mito		✓			2600	26	Xylose, aerobic, fed-batch	[17]	2019
Mito		✓			3100 ± 180	38.8 ± 2.4	Xylose, semi-aerobic, fed-batch	[18]	2019
Mito		✓		✓	167.2	3.4	Glucose, semi-aerobic, batch	[19]	2016
Cyto and mito		✓	✓		283 ± 13	11.46	Glucose, aerobic, batch	[20]	2017
Cyto and mito		✓			85.2	2.13	Glucose, anaerobic, batch	[21]	2011

Cyto = cytosolic-localization.
Mito = mitochondrial-localization.

isobutanol titers, demonstrating the importance of having a redox cofactor-balanced pathway (Table 1).

In this work, we aimed to provide insight into how pathway localization and redox cofactor-balancing affect the performance and physiology of isobutanol producing strains. We conducted a functional genomics analysis to elucidate differences between *S. cerevisiae* strains equipped with DNA cassettes that localized isobutanol biosynthesis to specific compartments, *i.e.* mitochondria vs. cytosol, and included either a NADPH-dependent (cofactor-imbalanced) or NADH-dependent (cofactor-balanced) KARI enzyme. Here, we report that pathway localization had a greater effect on isobutanol production than redox-balancing; the strain harboring the mitochondrial-localized isobutanol pathway outperformed the cytosolic version by 3.8-fold. The main limitation in the cytosolic-localization is the supply of the 2Fe–2S cluster cofactor for the DHAD enzyme; however, we found that this limitation may be partially overcome by increasing the availability of iron in the cell by perturbing iron homeostasis. Our findings contribute towards improving the metabolic engineering designs for building further improved isobutanol producing strains.

2. Materials and methods

2.1. Yeast media

Complex lab media for culturing, YP, consisted of 10 g/L yeast extract, 20 g/L peptone, and 20 g/L dextrose (YPD). 200 μg/mL Geneticin (US Biological, Swampscott, MA), 200 μg/mL Hygromycin B (US Biological, Swampscott, MA), 100 μg/mL Nourseothricin (Jena Bioscience, Jena, Germany), or 200 μg/mL Zeocin (Thermo Fisher Scientific, Waltham, MA) were added for maintenance of expression constructs where needed. Defined minimal medium contained 6.7 g/L yeast nitrogen base (YNB) without amino acids with ammonium sulfate, 19.5 g/L MES, 100 g/L dextrose, 4 mL/L 250X tween/ergosterol stock (62.5 mL Tween80 + 625 mg Ergosterol in 187 mL 95% EtOH) and pH adjusted to 5.5. Defined synthetic complete media contained 6.7 g/L yeast nitrogen base (YNB) without amino acids with ammonium sulfate, 1 g/L drop-out mix without yeast nitrogen base, and 20 g/L dextrose.

2.2. Cloning and yeast strain engineering

S. cerevisiae strains used in this study are described in Table S1. The parental WT strain [22] https://paperpile.com/c/CNM88o/8W7t was generated by transforming [23] a polymerase chain reaction (PCR) product containing the *URA*3 open reading frame (ORF), 225 bp of the 5′ UTR and 173 bp of the 3′ UTR from the GLBRCY22-3 strain ([24], G3) into the CEN.PK113-5D strain and plating on SC minus uracil plates. Transformants were confirmed for growth on auxotrophic medium without uracil and Sanger-sequenced. To generate strains expressing the isobutanol pathway genes, DNA containing codon-optimized versions of *ILV2*, *ILV3*, *ILV5* and *ARO10* from S. *cerevisiae*, and adhA^{29C8} from *Lactobacillus lactis* [25] were synthesized (Life Technologies) and cloned between various yeast promoters and terminators (together called the "isobutanol pathway cassette"). Specifically, expression was driven by the following promoter and terminator pairs: P_{ADH1}-*ILV2*-T_{CYC1}; P_{PGK1}-*ILV3*-T_{TEF2}; P_{TEF2}-*adhA*^{29C8}-T_{TDH3}; P_{TDH3}-*ARO10*-T_{TEF1}; P_{TEF1}-*ILV5*-T_{TUB1}. The P_{ADH1} consisted of 408 bp upstream of the *ScADH1* protein-coding sequence, T_{CYC1} consisted of 251 bp downstream of *ScCYC1* protein-coding sequence, P_{PGK1} consisted of 998 bp upstream of the *ScPGK1* protein-coding sequence, T_{TEF2} consisted of 293 bp downstream of the *ScTEF2* protein-coding sequence, P_{TEF2} consisted of 402 bp upstream of the *ScTEF2* protein-coding sequence, T_{TDH3} consisted of 514 bp downstream of the *ScTDH3* protein-coding sequence, P_{TDH3} consisted

of 672 bp upstream of the *ScTDH3* protein-coding sequence, T_{TEF1} consisted of 350 bp downstream of the *ScTEF1* protein-coding sequence, P_{TEF1} consisted of 577 bp upstream of the *ScTEF1* protein-coding sequence, T_{TUB} consisted of 380 bp downstream of the *ScTUB1* protein-coding sequence. The transcriptional units (promoter-gene--terminator pairs) for the five genes were then cloned in the above order into the *Sac*I-*Kpn*I polylinker sites of a modified pRS426 plasmid containing *HygMX4* as the selection marker in place of *URA3* [26]. Homology arms to the *HO* locus (*HO-L* and *HO-R*) were inserted 5′ and 3′ of the isobutanol pathway cassette to facilitate genome insertion by homologous recombination [27]. The *HO-R* homology arm also included the *LoxP-KanMX-LoxP* selection marker, which was inserted 3′ of *ScTUB1* protein-coding sequence [28]. For expressing *ARO10* and a*dhA*^{29C8} in the mitochondria, coding sequence for the *COX4* MLS was synthesized in-frame at the 5' ends of codon-optimized *ARO10* and *adhA*^{29C8}. The full length isobutanol pathway cassette containing mitochondrial-localized enzymes and flanking *HO* arms (GenBank: MZ541859) was excised from the plasmid by digestion with *Sac*I-HF and *Kpn*I-HF, purified and transformed into the WT strain. After selection on YPD + Geneticin plates, PCR and Sanger sequencing were used to confirm the insertion of the isobutanol pathway cassette into the *HO* locus. The *LoxP-KanMX-LoxP* selection marker was then excised by Cre recombinase to generate the final mIBA^{ILV5} strain [28]. The inserted isobutanol pathway cassette was amplified by PCR with multiple primer sets from mIBA^{ILV5} genomic DNA (gDNA) and confirmed for complete insertion by Sanger-sequencing (Fig. S1a). To generate the cIBA^{IlvC6E6} strain, CRISPR/Cas9 was used to delete the MLSs at the N-terminus of the engineered isobutanol pathway enzymes in mIBA^{ILV5} (Fig. S1b). In brief, an sgRNA sequence targeting the MLS of each synthetic isobutanol pathway enzyme were identified by CRISpy-pop [29] and cloned into the pXIPHOS plasmid as described previously [30]. sgRNA targeting sequences are as follows: *ILV2*, CTTAATAGCGAAGTTCTTCA; *ILV3*, AGTAGTAGAGAATTGTCTAG; *ILV5*, GCAGATCAATCTAGCAGCTT; *MLS-adhA*^{29C8} and *MLS-ARO10*, AAATCTGATGGACTGTCTCA. Each mitochondrial-localized gene in the synthetic isobutanol pathway was sequentially replaced by transforming the pXIPHOS plasmid containing a single sgRNA to one gene along with the appropriate PCR repair template of the gene lacking the MLS in the following order: *ILV5* - > *ilvC*^{6E6}, *MLS-ARO10* and *MLS-adhA*^{29C8} simultaneously - > *ARO10* and *adhA*^{29C8}, *ILV3* - > *ILV3*$^{\Delta 2\text{-}19}$, *ILV2* - > *ILV2*$^{\Delta 2\text{-}54}$. To generate repair templates with the cytosol-localized isobutanol pathway enzymes, individual genes were first cloned into the TOPO vector and then the appropriate MLS was removed (*ILV2*$^{\Delta 2\text{-}54}$, *ILV3*$^{\Delta 2\text{-}19}$, and *ILV5*$^{\Delta 2\text{-}48}$, *ARO10*$^{\Delta MLS}$, and *adhA*$^{29C8,\ \Delta 2\text{-}MLS}$ [6]) by restriction digestion/PCR-aided Gibson assembly and confirmed with Sanger-sequencing. These vectors were then used as the PCR repair template which contained part of the promoter and part of the gene lacking the MLS. The repair template for replacing *ILV5* with *ilvC*^{6E6} was generated by amplifying the *E. coli ilvC*^{6E6} CDS from pIBA1 [31] and cloning it in place of the ILV5$^{\Delta 2\text{-}48}$ CDS in the TOPO vector; this vector was Sanger-sequenced and used for the PCR repair template in the same manner as described earlier. To generate the cIBA^{ILV5} strain, the cIBA^{IlvC6E6} strain was transformed with the pXIPHOS plasmid containing an sgRNA to *ilvC*^{6E6} (AGTTTTAATTACAACCGGTA) and a PCR repair template containing *ILV5*$^{\Delta 2\text{-}48}$ (Fig. S1c). To generate the mIBA^{IlvC6E6} strain, the mIBA^{ILV5} strain was transformed with the pXIPHOS plasmid containing an sgRNA to codon-optimized *ILV5* (GCAGATCAATCTAGCAGCTT) and a PCR repair template containing *MLS-ilvC*^{6E6} (Fig. S1d). For the cIBA^{ILV5}, cIBA^{IlvC6E6} and mIBA^{IlvC6E6} strains, DNA sequence changes where CRISPR/Cas9 editing occurred were confirmed by Sanger-sequencing. Deletions of codon-optimized *ILV3*, native *ILV3* and/or native *FRA2* from the cIBA^{ILV5}, mIBA^{ILV5}, and cIBA^{IlvC6E6} strains were performed by integration of PCR products generated from *LoxP-KanMX-LoxP* (pUG6) or *LoxP-HphMX-LoxP* (pUG75) plasmid templates and primers containing 40–60 bp of homology flanking the targeted genes [32]. PCR products were purified and transformed into the appropriate strains and selected for growth on the appropriate antibiotic. Gene deletions were confirmed by PCR of gDNA and Sanger-sequencing.

2.3. Fermentation growth conditions and sample collection

For aerobic growth, starter cultures were grown in a shaking incubator at 30 °C. For anaerobic growth, media was allowed to degas in a 30 °C Coy anaerobic chamber (10% H_2, 10% CO_2, and 80% N_2) for >12 h prior to use and cultures were grown with stir bars on a magnetic stir plate to prevent flocculation. Fermentations for multi-omic sampling were performed in biological triplicate. Yeast cells were grown aerobically in YPD until stationary phase ~12 h. The cultures were then shifted to minimal medium and anaerobic conditions by diluting the culture to OD_{600} 0.3 in minimal medium and allowed to reach exponential phase ~8.5 h. Working cultures, which were used for sampling, were then inoculated from the shifted culture to OD_{600} 0.2 in minimal medium and allowed to grow anaerobically for 48 h. Cell growth was monitored by taking OD_{600} measurements with the Beckman DU720 spectrophotometer. Samples for end-product analysis were taken by collecting 2 mL of culture supernatant. Samples for protein isolation were obtained by collecting and flash freezing ~1×10^{11}/1×10^{12} cells. Similarly, samples for RNA isolation were obtained by collecting and flash freezing the equivalent of 25 mL of cells at an OD_{600} of 1. Samples for intracellular metabolite quantification were collected inside the anaerobic chamber by vacuum filtrations of culture through 0.45 μm hydrophilic nylon filters. Filters with the retained cells were immediately placed cell-side down in 1.5 mL of extraction solvent (40 vol% acetonitrile, 40 vol% methanol, 20 vol% water) kept on dry ice to quench metabolism and extract metabolites.

2.4. End-product analysis

2.4.1. Determination of isobutanol concentration by automated headspace GC/MS

The equipment used included the following: an Agilent 7890A GC system (Agilent Technologies, Inc. Palo Alto, CA); a LPAL3 autosampler and sample preparation system equipped with a heated agitator/stirrer and heated headspace sampling syringe (Agilent Technologies, Inc. Palo Alto, CA); and a Pegasus 4D ToF-MS (Leco Corp., Saint Joseph, Michigan). Typical analysis range is 0.065 mM–8.4 mM isobutanol and uses an aliquot volume of 500 mL and 2-Methylpropyl-d9 alcohol (as internal standard). Instrument run control and conditions are set by the Chromatof (®Leco Corp.) software (version 4.72.0.0) provided with the Pegasus 4D GcxGC ToF MS system. Samples were incubated at 70 °C for 5 min in the heated agitator set to 350 rpm. 0.5 mL of the headspace is then sampled by the autosampler with a 2.5 mL gastight syringe heated to 75 °C and injected into the GC system. The sample was withdrawn at 100 mL/s and injected into the GC at 1000 mL/s. The syringe was purged with nitrogen gas for 0.5 min prior to the next injection. The analytical capillary GC column was a Stabilwax-DA® (Restek, Inc. Bellefonte, PA) length 30 m, 0.25 mm ID, 0.25 mm film thickness. Helium was used as a carrier gas with a pressure corrected constant flow rate of 1 mL/min. The GC inlet was fitted with a 4 mm deactivated glass liner and held at 250 °C throughout the run. The inlet split ratio was set to 50:1. The GC oven was initially set to 50 °C and held for 1 min then increased to 200 °C at 40 °C/min and held at 200 °C for 5 min. The filaments of the mass spectrometer were turned on 42.5 s after injection and 10 spectra/sec were recorded from *m/z* 10 to *m/z* 250. The MS source temp was 200 °C, electron energy set to 70 eV, and the detector voltage was adjusted to approximately 50 V above the minimum voltage determined by the instrument tune check procedure. The peak area of isobutanol was measured using the extracted ion chromatogram of *m/z* 43 and the peak area of 2-Methylpropyl-d9 alcohol was measured from the extracted ion chromatogram of *m/z* 46. An unpaired *t*-test was performed to determine statistical significance.

2.4.2. Analysis of fermentation supernatants by HPLC-RID

End-product analytes (glucose, ethanol, glycerol, lactate, and acetate) were measured with an analytical system consisting of an Agilent 1260 Infinity HPLC system (Agilent Technologies, Inc., Palo Alto, CA) with a quaternary pump, chilled (4 °C) autosampler, vacuum degasser, refractive index detector, and a Aminex HPX-87H column with a Cation-H guard column (BioRad, Inc. Hercules, CA; 300 × 7.8 mm, cat# 125–0140). Operating parameters were as follows: 0.02 N H_2SO_4 mobile phase, 0.500 mL/min flow rate, 50 °C column temperature, 50 °C detector temperature, 28 min run time, and a 50 μL injection volume. Instrument control, data collection and analysis/calculation are done using Chem Station V. B04.03 software (Agilent Technologies, Inc., Palo Alto, CA). An unpaired *t*-test was performed to determine statistical significance.

2.5. Intra- and extra-cellular metabolomics preparation, quantification, and analysis

After collecting all samples at a given time point, the filter disks in extraction solvent were removed from the anaerobic chamber and the cells were washed off the filter into the solvent. The entire suspension was transferred into a centrifuge tube and centrifuged for 5 min at 16,000×*g* at 4 °C to remove cellular debris. The supernatant was collected in another centrifuge tube and immediately prepped for quantification.

The extraction solvent containing intracellular metabolites was dried under N_2 and the metabolites were resuspended in Solvent A (97:3H_2O: methanol with 10 mM tributylamine adjusted to pH 8.2 by addition of 10 mM acetic acid). Samples were analyzed by LC-MS as described previously [33,34]. Data analysis was performed using MAVEN software [35,36] and compounds were identified by retention time (matched to pure standards). "Peak Area Top" values were extracted and normalized by OD_{600} equivalent of sample injected into the LC-MS. Extracellular metabolite samples for LC-MS analysis were diluted to appropriate concentration, then analyzed using the above method. An unpaired *t*-test was performed to determine statistical significance.

2.6. Transcriptomic sample preparation, library construction, sequencing, and analysis

Total RNA was extracted with hot phenol lysis [37], DNA was digested with Turbo-DNase (Life Technologies, Carlsbad, CA) for 30 min at 37 °C, and RNA was precipitated with 2.5 M LiCl for 30 min at 20 °C. In brief, RNA-Seq libraries were generated using the Illumina TruSeq® Stranded mRNA HT kit, AMPure XP bead for PCR purification (Beckman Coulter, Indianapolis, IN), and SuperScriptII reverse transcriptase (Invitrogen, Carlsbad, CA) as described in the Illumina kit. Single-end 50-bp reads were generated using an Illumina NovaSeq 6000 at the University of Wisconsin-Madison Biotechnology Center. Reads were processed with Trimmomatic version 0.3 [38] and mapped to the S288C genome (with foreign mutant sequences added) using Bowtie 2 version 2.2.2 with default settings [39]. Read counts were calculated using HTseq version 0.6.0 [40]. edgeR version 3.6.8 [41] was used to perform differential gene analysis, taking a Benjamini and Hochberg false discovery rate (FDR) of <0.05 as significant [42]. Raw sequencing counts were normalized using Trimmed Means of M-values (TMM). Samples were clustered using Cluster 3.0 [43] and visualized in Java TreeView [44], and functional GO term enrichment was performed using SetRank [45] with an FDR set to < 0.05 for significance.

2.7. Label-free quantitative proteomics preparation, quantification, and analysis

Yeast pellets were resuspended in 150 μL of 6 M guanidine, 100 mM Tris (pH 8) and boiled for 5 min at 100 °C. Methanol was then added to 90% to precipitate proteins, and the samples were centrifuged for 5 min at 9,000 G. The supernatant was discarded, and the protein pellet was resuspended in lysis buffer (8 M urea, 100 mM Tris pH 8, 20 mM TCEP, 80 mM Chloroacetamide). LysC was added to an estimated 50:1 protein to enzyme ratio and incubated for 4 h at room temperature. The samples were diluted with 100 mM Tris to a urea concentration of 1.5 M. Trypsin was added to an estimated 50:1 protein to enzyme ratio and incubated overnight at room temperature. Samples were desalted with Strata C18 solid phase extraction cartridges and dried in a vacuum centrifuge. Peptide concentration was then determined from a NanoDrop One spectrophotometer before re-suspending in 0.2% formic acid and injecting onto the mass spectrometer.

Samples were analyzed using an LC-MS/MS instrument comprising an Orbitrap Eclipse Tribrid mass spectrometer and UltiMate 3000 RSLCnano liquid chromatography system (Thermo Fisher Scientific). Mobile phase A consisted of 0.2% formic acid in water and mobile phase B consisted of 0.2% formic acid in 80% acetonitrile. Peptides were loaded in 0% B and separated at a flow rate of 310 nL/min over a 120 min gradient of increasing % B. Peptides were injected onto a 1.7 μm C18 column (75 μm i.d.) packed in-house to a length of 30 cm [46] and heated to 50 °C. Survey scans of peptide precursors were collected every second from 300 to 1350 Th with an AGC target of 1,000,000 and a resolution of 240,000 in the orbitrap. Precursors were isolated from a 0.5 Th window in the quadrupole and HCD MS/MS scans at 35% collision energy were collected in the ion trap with an AGC target of 35,000 from 150 to 1350 Th.

The resulting LC-MS/MS proteomics data were processed using MaxQuant [47] software version 1.5.2.8 and searched against a *Saccharomyces cerevisiae* database (with foreign mutant proteins added) downloaded from Uniprot. The digestion enzyme was set to Trypsin/P with up to two missed cleavages, and oxidation of methionine and protein N-terminal acetylation were set as variable modifications. Cysteine carbamidomethylation was set as a fixed modification. Label-free quantification was enabled with a minimum ratio count of 1, and the match between runs feature was utilized to decrease missing data values within the dataset. Peptides were filtered to a 1% FDR and combined to protein groups based on the rules of parsimony. Differential protein analysis was done taking a Benjamini and Hochberg false discovery rate (FDR) of <0.05 as significant [42]. Functional enrichment was assessed using the FunSpec database [48].

2.8. Petite frequency

To assess the propensity of different strains to form petite colonies due to loss of respiratory competence each strain was revived on YPD media and streaked for single colonies on YPG (2% glycerol) media to ensure all starting cells could respire. Single colonies were used to inoculate 3 independent 5 mL YPD cultures, which were grown rolling overnight at 30 °C. Each culture was plated for single colonies on YPDG (0.1% dextrose, 3% glycerol) media to differentiate petite and respiring colonies and colonies were counted after 3 days of growth at 30 °C.

3. Results and discussion

3.1. Engineered isobutanol producing strains

In order to evaluate the effects of pathway localization and redox cofactor-balancing on isobutanol production, we constructed four engineered strains: a mitochondrial-localized isobutanol pathway with a NADPH-dependent Ilv5p KARI, $mIBA^{ILV5}$; a mitochondrial-localized isobutanol pathway with a NADH-dependent $IlvC^{6E6}$p KARI, $mIBA^{IlvC6E6}$; a cytosolic-localized isobutanol pathway with a NADPH-dependent Ilv5p KARI, $cIBA^{ILV5}$; and a cytosolic-localized isobutanol pathway with a NADH-dependent $IlvC^{6E6}$p KARI, $cIBA^{IlvC6E6}$ (Fig. 1b and c, Table S1/Fig. S1, Materials and methods 2.2). DNA cassettes for expressing each pathway were assembled from genes previously tested [5], including those encoding an alcohol dehydrogenase ($adhA^{29C8}$, from

Lactococcus lactis [25]), an acetolactate synthase (*ILV2*, from *S. cerevisiae*), a dihydroxyacid dehydratase (*ILV3*, from *S. cerevisiae*), a α-ketoacid decarboxylase (*ARO10*, from *S. cerevisiae*), and a ketol-acid reductoisomerase (*ILV5*, from *S. cerevisiae or ilvC*^{6E6}, from *E. coli* [31]). Each open reading frame was codon-optimized, synthesized commercially, and cloned in frame with promoters (P) and terminators (T) resulting in the following pairs: P_{ADH1}-*ILV2*-T_{CYC1}; P_{PGK1}-*ILV3*-T_{TEF2}; P_{TEF2}-*adhA*^{29C8}-T_{TDH3}; P_{TDH3}-*ARO10*-T_{TEF1}; P_{TEF1}-*ILV5*-T_{TUB1}; P_{TEF1}-*ilvC*^{6E6}-T_{TUB1} (Materials and methods 2.2). Mitochondrial localization was achieved by adding DNA encoding the previously characterized Cox4p N-terminal MLS [5] to the N-terminus of genes which natively localized to the cytosol (*MLS-ARO10*, *MLS-adhA*^{29C8}, and *MLS-ilvC*^{6E6}). Conversely, cytosol targeting was achieved by removing sequences encoding previously identified MLS from genes which natively localized to the mitochondria (*ILV2*$^{\Delta 2\text{-}54}$, *ILV3*$^{\Delta 2\text{-}19}$, and *ILV5*$^{\Delta 2\text{-}48}$) [6]. DNA cassettes containing each of the five genes were assembled and integrated into the *S. cerevisiae* genome at the *HO* locus via homologous recombination. When constructing the mIBA^{IlvC6E6} strain we uncovered an unexpected petite phenotype. The frequency at which the petite colonies arose in the mIBA^{IlvC6E6} strain was 166-fold that of the wild-type (WT) strain (Table S2). All other engineered strains had a low petite frequency consistent with natural *S. cerevisiae* isolates [49,50]. The mIBA^{IlvC6E6} strain was not included in further studies due to this irreversible fitness defect.

3.2. Engineered strains produce varied amounts of isobutanol

A fermentation experiment was performed to evaluate and compare the physiological and molecular phenotypes of the engineered strains and WT. Each strain was cultivated anaerobically at 30 °C in minimal medium containing 100 g/L glucose. We collected samples every 2 h to monitor growth, glucose consumption, isobutanol production, and ethanol production. Samples for functional genomics analyses (transcriptomic, proteomic and metabolomic) were collected at 4, 10, and 26 h post inoculation to represent the different phases of cell growth: early-exponential phase, mid-exponential phase, and early-stationary phase (Fig. 2). The three engineered strains grew slower than the WT strain (Fig. 2); doubling times during the exponential phase of the mIBA^{ILV5}, cIBA^{ILV5} and cIBA^{IlvC6E6} strains were 1.1, 1.3, and 1.3-fold larger than the WT strain, respectively. All strains completely consumed the glucose provided and reached similar final OD_{600} (5.3–5.6) values by the end of the 48 h fermentation. All strains produced ethanol titers of 45–47 g/L by44 h of the fermentation corresponding to yields over 90% of the theoretical maximum (Fig. 2). These metrics indicate that ethanol remains the dominant fermentation product and that pathway localization and cofactor-balance alone were not the limiting factor in isobutanol fermentation.

Isobutanol production varied significantly among the engineered strains. The cIBA^{ILV5} and cIBA^{IlvC6E6} strains produced isobutanol at levels less than or equal to WT; at 38 h, the isobutanol titers were 37, 46, and 31 mg/L in the WT, cIBA^{ILV5}, and cIBA^{IlvC6E6} strains, respectively. The cIBA^{ILV5} strain produced 1.5-fold ($P < 5E\text{-}5$) more isobutanol than the cIBA^{IlvC6E6} strain indicating that redox cofactor-balancing is not a limiting factor for driving flux to isobutanol synthesis in these strains and NAD^+ is preferentially regenerated through ethanol fermentation. The highest isobutanol titer was achieved by the mIBA^{ILV5} strain, which produced 170 mg/L at 38 h, corresponding to a yield of 1.8 mg isobutanol/g glucose. This metric is similar to other isobutanol overproducing strains grown under anaerobic conditions [21]. In summary, the mIBA^{ILV5} strain outperforms the other engineered strains and had a 3.8-fold ($P < 5E\text{-}6$) higher isobutanol titers than the cIBA^{ILV5} strain.

3.3. Strains with cytosolic-localized isobutanol pathway have an altered transcriptome and proteome

We next assessed the molecular phenotypes of the engineered strains and WT using the functional genomics samples collected during the above-mentioned fermentation experiment. We identified and collected data for 59 intracellular metabolites using LC-MS, 34 extracellular metabolites (28 LC-MS and 6 HPLC/GC), 4339 proteins by LC-MS/MS proteomics, and 6434 genes by RNA-seq (File S1–S4, Data availability).

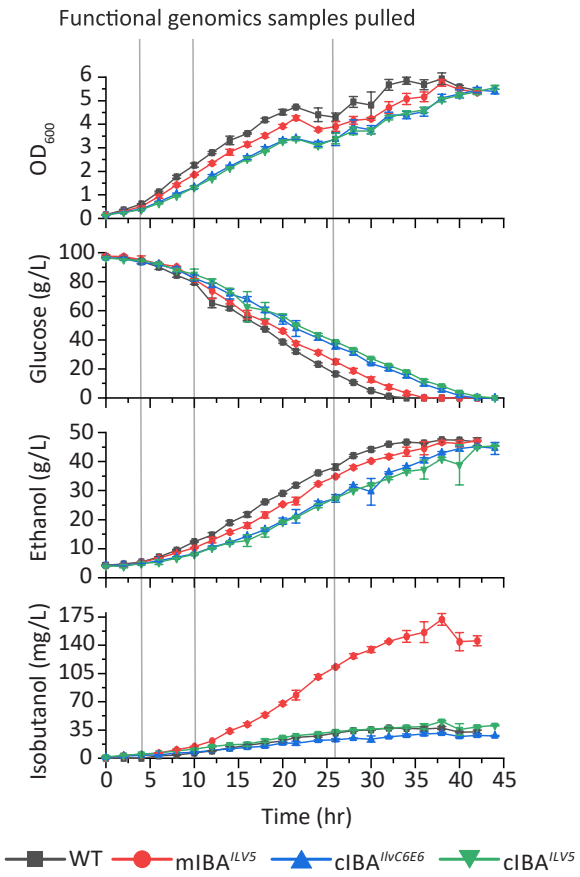

Fig. 2. Mitochondrial-localized isobutanol pathway is sufficient for increasing isobutanol titers. Fermentation was performed on the isobutanol producing *S. cerevisiae* strains under anaerobic conditions in minimal medium for 48 h. Cell growth (OD_{600}), glucose, ethanol and isobutanol production were measured. Error bars represent the standard deviation of three biological replicates. Samples for functional genomics analysis (proteomics, transcriptomics, and metabolomics) were pulled at 4, 10, and 26 h indicated by vertical gray lines.

The transcriptome and proteome data collected from our top isobutanol producer, mIBA^{ILV5}, was more similar to WT than the cIBA^{IlvC6E6} and cIBA^{ILV5} strains which both displayed a larger number of differentially expressed RNA and proteins (Fig. 3a, Table S3). The cIBA^{IlvC6E6} and cIBA^{ILV5} strains shared 175 of the same differentially expressed genes, which were enriched for oxidation-reduction processes, mitochondrial respiration, and TATA-containing genes (Fig. 3b). Hierarchical clustering of the data was also performed, and the strains clustered together in a distinct clade within each timepoint (Fig. 3c). Taken together, we concluded that the cIBA^{IlvC6E6} and cIBA^{ILV5} strains have functionally similar transcriptomes and that a cytosolic-localized isobutanol pathway induces gene expression changes in specific biological processes.

The metabolite dataset showed that all engineered strains had significantly altered levels of aromatic amino acid biogenesis intermediates (Fig. S2 and Fig. S3). We suspect this was due to overexpression of the synthetic KDC enzyme, Aro10p, in our engineered strains enhancing aromatic amino acid degradation flux (Fig. S3). The depletion of phenylalanine (Phe) and tyrosine (Tyr) did not cause any unexpected changes in cell growth as supplementation with 0.1% (w/v)

a.

Strains	Differentially expressed genes at an reduced level	Differentially expressed genes at an elevated level
mIBA^{ILV5}	0	0
cIBA^{IlvC6E6}	105	110
cIBA^{ILV5}	224	234

b.

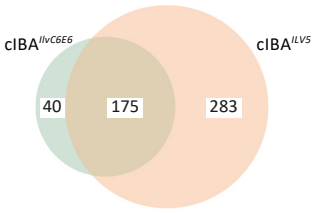

*No significant DE genes between mIBA^{ILV5} and WT

Enriched ovelapping genes in cIBA^{ILV5} and cIBA^{IlvC6E6}
TATA-containg genes
Mating
Oxidation-reduction process
Hydrogen ion transmembrane transport
Mitochondrial electron transport, ubiquinol to cytochrome C

c.

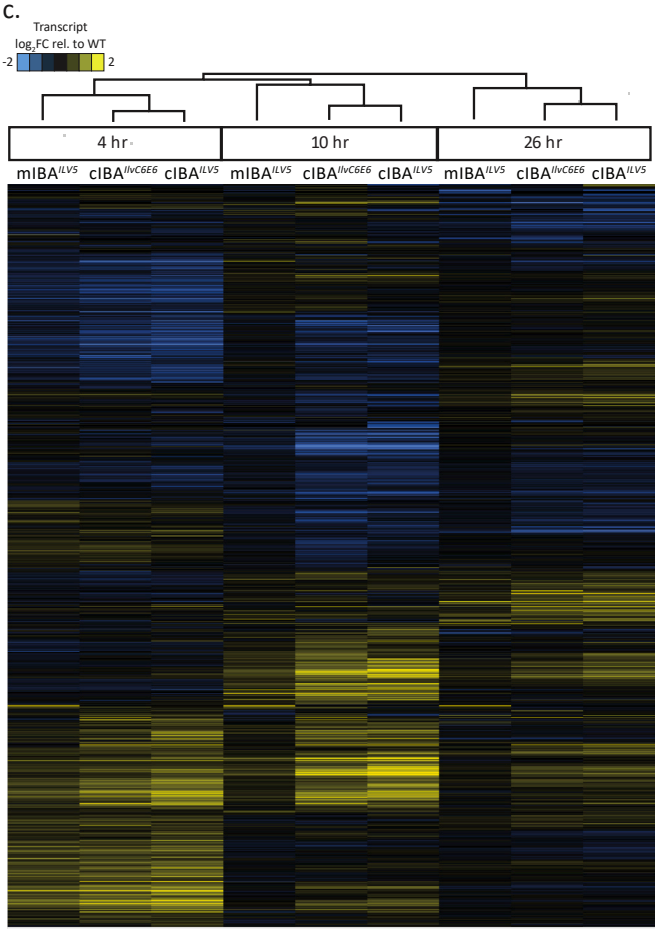

Fig. 3. Transcriptomics overview of the engineered isobutanol strains. a) Number of differentially expressed genes at an elevated or reduced level in the engineered strains relative to WT **b)** Venn Diagram showing the number of overlapping differentially expressed genes in the cIBA^{IlvC6E6} and cIBA^{ILV5} strains and the GO terms enrichment results (Bonferroni adjusted $P < 1E-05$). **c)** Heatmap shows the average relative Log_2 fold change of genes (rows) for each strain/time point (columns) relative to WT. The three sampling times were early-exponential phase (4 h), mid-exponential phase (10 h), and early-stationary phase (26 h) for strains mIBA^{ILV5}, cIBA^{ILV5}, and cIBA^{IlvC6E6} grown in minimal medium anaerobically. Yellow denotes induced expression, blue denotes repressed expression, and black denotes unchanged values according to the key. Hierarchical clustering was performed with Cluster 3.0 and visualized in Java TreeView (Materials and methods 2.6). The transcriptome of the cIBA^{ILV5} and cIBA^{IlvC6E6} strains were more similar than the mIBA^{ILV5} strain. (For interpretation of the references to colour in this figure legend, the reader is referred to the Web version of this article.)

Phe and Tyr yielded no improvement in growth rate (Fig. S4). Metabolites in the IBA pathway were also dramatically altered but more so in the cIBA^{IlvC6E6} and cIBA^{ILV5} strains when compared to WT (Fig. S2). The remainder of the manuscript will discuss conclusions we drew after integrating specific aspects of the functional genomics data.

3.4. Cytosolic-localized isobutanol pathway has a bottleneck at Ilv3p

We first examined data related to enzymes in the isobutanol pathway. To judge if each of our synthetic enzyme variants was expressed, the mRNA counts and protein abundance data were investigated. Normalized counts (RPKM) for all synthetic codon-optimized isobutanol genes (*ILV2, ILV2$^{\Delta 2\text{-}54}$, ILV5, ILV5$^{\Delta 2\text{-}48}$, ilvC^{6E6}, ILV3, ILV3$^{\Delta 2\text{-}19}$, MLS-adhA^{29C8}, adhA^{29C8}, MLS-ARO10, and ARO10)* were successfully detected in the transcriptomes of the engineered strains (Table S4). In general, the amount of RNA detected for each transcript correlated with the predicted promoter strengths of each gene (P_{THD3}-*ARO10* > P_{PGK1}-*ILV3* > P_{TEF1}-*ILV5/ilvC^{6E6}* > P_{TEF2}-*adhA^{29C8}* > P_{ADH1}-*ILV2*) (Table S4) [51,52]. The transcript levels of the native *ILV2, ILV5, ILV3*, and *ARO10* genes were also investigated, and as expected, the mRNA abundances of the native genes were not statistically significantly altered in any of the engineered strains compared to the WT strain (File S1). The protein levels of the isobutanol enzymes (Ilv2p, Ilv3p, Ilv5p, and Aro10p) were elevated across all the engineered strains when compared to WT (Fig. 4). This elevated protein abundance in our engineered strains can be a result of our synthetic variants being successfully translated and contributing to the protein pool. Overall, neither the mRNA counts nor the protein abundance data yielded an explanation for the differences in isobutanol production we observed between the engineered strains. We contribute the higher isobutanol production in the mIBA^{ILV5} strain to be the result of added activity from the mitochondrial pathway localization.

Next, we looked at the intracellular levels of the isobutanol pathway intermediates in our engineered strains and saw that 2-acetolactate (AL), 2,3-dihydroxyisovalerate (DHIV), and α-ketoisovalerate (KIV) were significantly altered compared to the WT strain. At 4 h, the cIBA^{ILV5} strain had a 23-fold ($P < 5.0E-4$), 16-fold ($P < 5.0E-5$), and 4.1-fold ($P < 0.005$) increase in intracellular AL, DHIV, and KIV, respectively when compared to WT. Similarly, at 4 h, the cIBA^{IlvC6E6} strain had a 22-fold ($P < 5e-6$), 8.6-fold ($P < 0.0005$), and 2.5-fold ($P < 5E-4$) increase in intracellular AL, DHIV, and KIV, respectively when compared to WT (Fig. 5). This trend of elevated intracellular AL, DHIV, and KIV in the cIBA^{IlvC6E6} and cIBA^{ILV5} strains was also seen at the other timepoints, 10 and 26 h, but to a lesser extent. The significant accumulation of AL and DHIV in these strains indicates that *ILV3* is a rate-limiting step. This finding was also in agreement with a previous study where additional

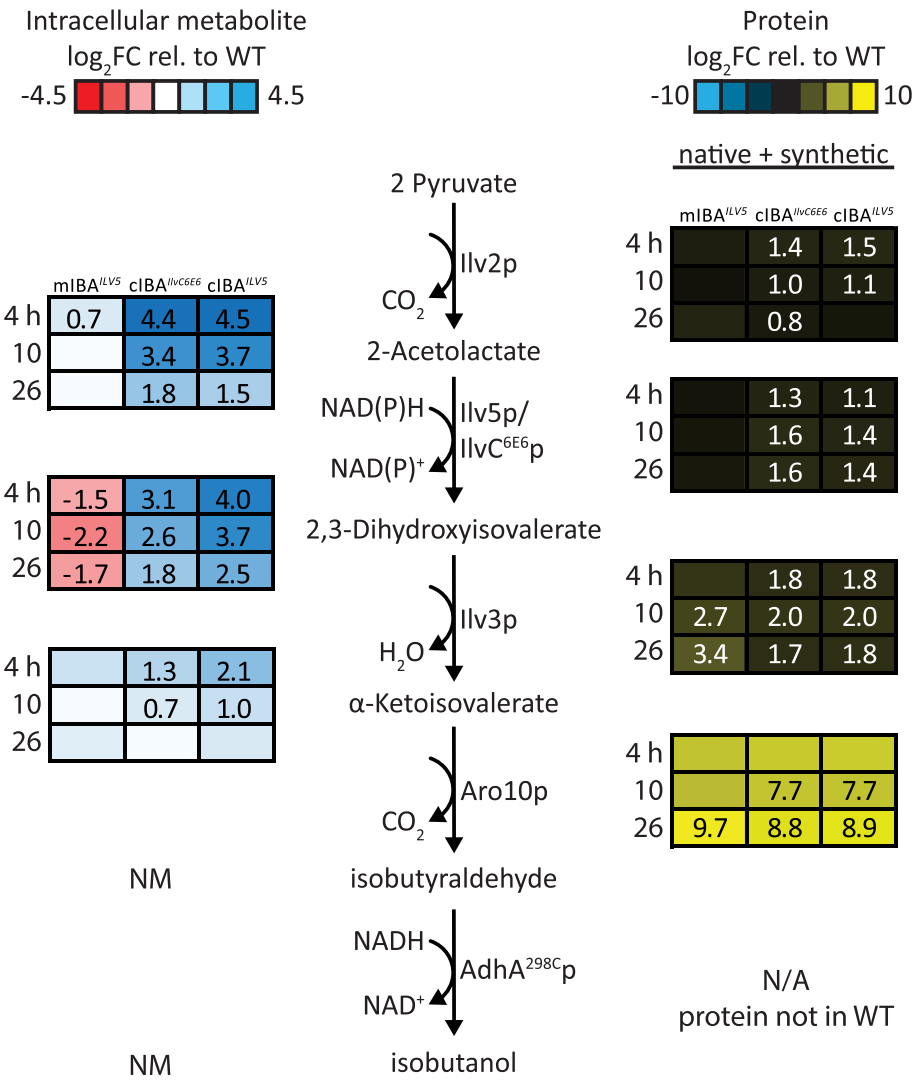

Fig. 4. Intracellular metabolite and protein levels of the isobutanol pathway. Heat map values correspond to average Log_2 fold change relative to WT at the 3 sampling times (4, 10, and 26 h). For the intracellular metabolite data, red denotes lower metabolite levels, blue denotes higher metabolite levels, and white denotes unchanged values; for the protein data, blue denotes lower protein levels, yellow denotes higher protein levels, and black denotes unchanged values. Protein values represent the sum of the native and synthetic proteins. Statistical significance (P/FDR <0.05) is indicated by the presence of a number in the heatmap cell. NM stands for not measured, and N/A stands for not applicable as the protein is not endogenous to WT. (For interpretation of the references to colour in this figure legend, the reader is referred to the Web version of this article.)

copies of *ILV3* were added to boost production of KIV from DHIV [15]. In contrast to the cIBA^{IlvC6E6} and cIBA^{ILV5} strains, intracellular levels of DHIV in the mIBA^{ILV5} strain were at lower levels compared to the WT strain; specifically, the level of DHIV was 2.8-fold (P < 5E-4), 4.5-fold (P < 0.005), and 3.2-fold (P < 0.005) lower when compared to WT at 4, 10, and 26 h respectively, which indicates mitochondrial-localized Ilv3p is not a bottleneck.

We hypothesized that the mitochondrial-localized Ilv3p is not a rate-limiting step in the mIBA^{ILV5} strain because the required cofactor for the enzyme, a 2Fe–2S cluster, is more accessible in the mitochondria where its biogenesis begins. This is not the case for the cIBA^{IlvC6E6} and cIBA^{ILV5} strains since the synthesis and delivery of the required 2Fe–2S cluster into the cytosolic-localized Ilv3p requires Fe–S cluster biogenesis machinery that spans multiple compartments (both the mitochondria and cytosol). Specifically, the mitochondrial iron sulfur cluster (ISC) machinery is responsible for generating the sulfur-containing intermediate (X–S), which is then exported to the cytosol via the ABC transporter Atm1p [53]. In the cytosol, the X–S intermediate is matured into a cluster and loaded onto the cytosolic-localized apoprotein by the cytosolic iron sulfur cluster assembly (CIA) machinery (Fig. 5a). We hypothesized that the Ilv3p step is rate-limiting in the cIBA^{IlvC6E6} and cIBA^{ILV5} strains due to this added complexity of the cross-compartmental assembly of the required cofactor. To confirm that our cytosolic-localized Ilv3p was functional, we deleted the endogenous mitochondrial-localized *ILV3* in the cIBA^{IlvC6E6} strain and performed a growth complementation assay to see if our synthetic cytosolic-localized Ilv3p could restore growth on synthetic complete medium lacking valine; indeed, the strain harboring only the cytosolic-localized Ilv3p grew on synthetic complete medium minus valine plates indicating it was functional in its non-native subcellular compartment (Fig. S5). In summary, the lower performance of the strain with the cytosolic-localized pathway was due to a rate-limiting step in the pathway at Ilv3p.

3.5. Proteomics analysis revealed a cytosolic-localized isobutanol pathway results in altered sulfur metabolism

To further explore our hypothesis that the Fe–S cluster requiring enzyme was the rate-limiting step in the cIBA^{IlvC6E6} and cIBA^{ILV5} strains, we took a closer look at genes involved in Fe–S cluster synthesis. The protein levels of enzymes in the ISC and CIA machinery between the engineered strains and WT were relatively unchanged, with the exception of Atm1p, the mitochondrial X–S intermediate transporter (Table S5). Atm1p was upregulated approximately 2.0-fold in the cIBA^{IlvC6E6} and cIBA^{ILV5} strains at all time points when compared to WT (Fig. 5b). Atm1p overexpression is predicted to increase the number of available clusters in the cytosol by increasing the abundance of the X–S intermediate used by the CIA machinery for generating cytosolic Fe–S clusters [53]. In the cytosol, excess Fe–S clusters are sensed by the iron responsive transcription factor, Yap5p. Yap5p can stably bind to 2Fe–2S

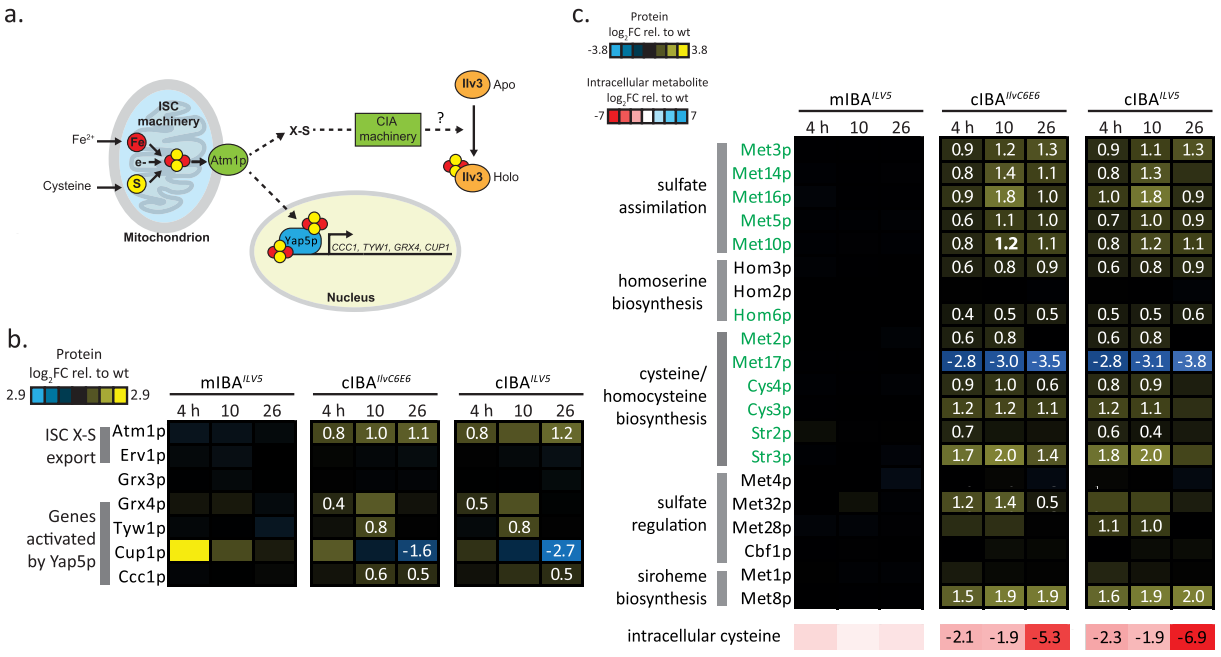

Fig. 5. Proteomics response of sulfur-related pathways in the engineered strains a) Model for cytosolic 2Fe–2S cluster biogenesis, delivery, and sensing. Fe–S cluster biogenesis begins with the mitochondrial iron sulfur cluster (ISC) machinery where a sulfur containing compound (X–S) is made and exported to the cytosol via the ABC transporter, Atm1p. Through a yet unknown mechanism, the X–S intermediate is matured into a 2Fe–2S cluster and loaded into the cytosolically localized DHAD/Ilv3p apoprotein to form the holo form; we hypothesize that this process is facilitated by the cytosolic iron sulfur cluster assembly (CIA) machinery. High cytosolic iron conditions are sensed by the transcription factor Yap5p via binding two 2Fe–2S clusters; once clusters are bound, Yap5p undergoes a conformational change and activates transcription of genes in the nucleus including *CCC1*, *TWY1*, *GRX4*, and *CUP1*. **b)** Heat map shows the protein levels of such genes in model a. **c)** Heat map shows the protein levels of genes in sulfur-related pathways and the intracellular level of cysteine. Genes that are transcriptionally activated by Met4p under cysteine-depleted conditions are indicated in green. For all heatmaps, values correspond to average Log_2 fold change relative to WT at the 3 timepoints (4, 10, and 26 h). For the protein data, blue denotes lower protein levels, yellow denotes higher protein levels, and black denotes unchanged values. For the intracellular metabolite data, red denotes lower metabolite levels, blue denotes higher metabolite levels, and white denotes unchanged values. Statistical significance (*P*/FDR <0.05) is indicated by the presence of a number in the heatmap cell. (For interpretation of the references to colour in this figure legend, the reader is referred to the Web version of this article.)

clusters, inducing a conformational change that activates the transcription of genes to help regulate iron storage including *CCC1*, *TWY1*, *GRX4*, and *CUP1* (Fig. 5a). Indeed, protein levels of Ccc1p, Tyw1p, and Grx4p were elevated in the cIBA^{IlvC6E6} and cIBA^{ILV5} strains for at least one of the time points with Tyw1p having the highest fold change of 1.7 at10 h when compared to WT (Fig. 5b). This increase in Yap5p responsive genes indicated there was an increased number of 2Fe–2S clusters in the cytosol of the cIBA^{IlvC6E6} and cIBA^{ILV5} strains compared to WT, which was expected with the increased level of Atm1p.

We next asked if the different isobutanol pathways could affect other aspects of the strain's proteome. Pathway enrichment analysis using Funspec [48] was performed on the statistically significant protein hits from the cIBA^{IlvC6E6} and cIBA^{ILV5} strains to identify any enriched patterns. Proteins at a higher abundance compared to WT were enriched (P < 5E-5) for sulfur-related pathways (methionine biosynthesis [GO:0009086], cysteine biosynthesis [GO:0019344], and sulfate assimilation [GO:0000103]) (File S5). The protein abundance of enzymes in sulfate assimilation, sulfate regulation, homoserine biosynthesis, cysteine biosynthesis, and siroheme biosynthesis pathways were elevated in the cIBA^{IlvC6E6} and cIBA^{ILV5} strains compared to WT (Fig. 5c). This response was largely due to the depletion of intracellular cysteine since *MET* gene expression is induced by Met4p under cysteine-limited conditions [54]; in fact, the intracellular cysteine levels were depleted in all engineered strains but more significantly in the cIBA^{IlvC6E6} and cIBA^{ILV5} strains (Fig. 5c). Cysteine is used as the sulfur donor for synthesizing Fe–S clusters, and we hypothesized the altered sulfur metabolism was related to the 2Fe–2S cluster requirement of the rate-limiting enzyme, Ilv3p. The elevated levels of Atm1p in conjunction with the elevated sulfur metabolism suggests that the strains with the cytosolic pathway are trying to overcome a limitation in the quantity of cytosolic Fe–S clusters. We hypothesize that the insufficient availability of cytosolic Fe–S clusters causes the Ilv3p to be the bottleneck in the cIBA^{IlvC6E6} and cIBA^{ILV5} strains.

3.6. *Increasing iron availability boosts production with a cytosolic-localized pathway*

We next sought to determine if the cIBA^{IlvC6E6} and cIBA^{ILV5} strains' performance would benefit from increased Fe–S cluster biogenesis in the cell. This strategy was successful in increasing the activity of a different cytosolic-localized Fe–S cluster requiring enzyme, xylonate dehydratase, in *S. cerevisiae* [55,56]. This can be accomplished by increasing the availability of iron in the cell through deregulation of the iron regulon genes. To test our hypothesis, we disrupted iron homeostasis by deleting the transcriptional repressor Fra2p (also referred as its standard name Bol2p) of the iron regulon transcriptional activator, Aft1/2p, in the cIBA^{ILV5} and mIBA^{ILV5} strains (Fig. 6a) [53,57]. We then performed a time-course experiment where extracellular isobutanol production was monitored periodically and intracellular isobutanol metabolites were measured during mid-exponential phase (10 h) and early-stationary phase (26 h) (Fig. 6b and c). We observed that the deletion of *FRA2* significantly altered the isobutanol titer in the cIBA^{ILV5} background strain, but not in the mIBA^{ILV5} strain; the cIBA^{ILV5} *fra2Δ* strain produced 190 mg/L isobutanol at 48 h which is 2.4-fold more than the cIBA^{ILV5} strain (P < 5E-5) (Fig. 6b). Furthermore, the titer achieved by the cIBA^{ILV5} *fra2Δ* strain surpassed the isobutanol titer in our previous best producer, mIBA^{ILV5}, by 1.3-fold (P < 5E-5) indicating a high titer with a cytosolic isobutanol pathway localization can be achieved. We

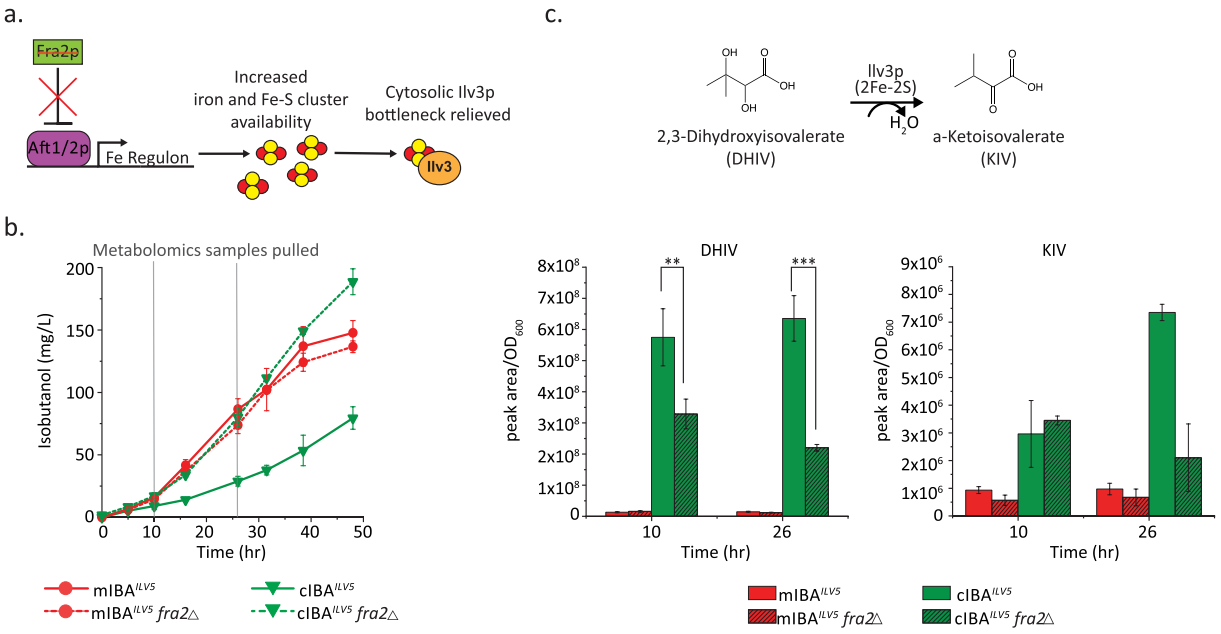

Fig. 6. Increasing iron availability improves isobutanol production with cytosolic-localized pathway a) Schematic demonstrating how Ilv3p activity may be enhanced by altering iron homeostasis. The transcriptional activator, Aft1/2p, is negatively regulated by Fra2p. **b)** Isobutanol titer of engineered isobutanol producing strains with and without *FRA2* deletion. **c)** Normalized peak area (peak area/OD_{600}) of Ilv3p's metabolites (reactant DHIV and product KIV) observed by LC-MS. Samples for metabolomics were pulled at 10 and 26 h post inoculation. Fermentation was performed under anaerobic conditions in minimal medium. Error bars represent the standard deviation of three biological replicates. Asterisks denote statistically significant differences by pairwise *t*-test (*, $P < 0.05$; **, $P < 0.005$; ***, $P < 0.0005$).

hypothesize the *fra2* deletion had no effect on isobutanol titer in the $mIBA^{ILV5}$ strain because the cofactor availability for the mitochondrial-localized Ilv3p was not limited.

We next tested if the deletion of *FRA2* specifically benefited Ilv3p by looking at the intracellular metabolite levels of the enzyme's reactant, DHIV, and product, KIV (Fig. 6c). Indeed, the $cIBA^{ILV5}$ *fra2Δ* strain had lower levels of DHIV compared to the $cIBA^{ILV5}$ strain indicating the Ilv3p bottleneck was partially relieved; the normalized peak area (peak area/OD_{600}) of DHIV was 1.7-fold ($P < 0.05$) and 2.9-fold ($P < 0.005$) lower in $cIBA^{ILV5}$ *fra2Δ* compared to $cIBA^{ILV5}$ at 10 and 26 h, respectively. The KIV level was also measured, but we did not observe an increased level of KIV in the $cIBA^{ILV5}$ *fra2Δ* strain compared to the $cIBA^{ILV5}$ strain as one might expect from relieving the bottleneck at Ilv3p. Instead, the KIV level between the engineered strains was not significantly altered, except at 26 h where the $cIBA^{ILV5}$ strain had a 3.5-fold increase in KIV compared to the $cIBA^{ILV5}$ *fra2Δ* strain ($P < 0.05$). We suspect an accumulation of KIV was not seen because KIV is readily consumed in the subsequent step. Taken together, the *fra2* mutation in the $cIBA^{ILV5}$ strain resulted in an increase in isobutanol titer, potentially by partially overcoming the 2Fe–2S cluster cofactor limitation for cytosolic Ilv3p.

4. Conclusions

Here, we combined transcriptomic, proteomic, and metabolomic analyses to generate a wealth of data on how enzyme pathway localization and redox cofactor-balancing affect isobutanol biosynthesis and physiology in genetically engineered *S. cerevisiae*. Localizing isobutanol pathway enzymes to the mitochondria resulted in higher titers, while cytosolic localization resulted in much lower titers. Metabolomic analysis uncovered a potential limitation in cytosolic Fe–S cluster biogenesis. This limitation could be overcome by increasing Fe uptake through deletion of *FRA2*. This strategy of increasing the availability of iron in the cell was also successful in increasing the activity of another Fe–S cluster requiring enzyme xylonate dehydratase; however, this strategy may not be effective for all Fe–S cluster requiring enzymes as this strategy had no effect on 6-phosphogluconate dehydratase activity [55, 58]. While we did not observe a beneficial effect in having a redox cofactor-balanced isobutanol pathway, we hypothesize that the cofactor imbalance will have to be resolved for the capacity of the isobutanol pathway to be enhanced. Furthermore, any problems caused by an imbalance will be exacerbated when ethanol flux is displaced to enhance the rate of isobutanol synthesis. Future functional genomics studies with engineered strains disabled for ethanol production should uncover new genetic targets for achieving greater isobutanol titers and yields.

Funding information

This material is based upon work supported by the Great Lakes Bioenergy Research Center, U.S. Department of Energy, Office of Science, Office of Biological and Environmental Research under Award Number DE-SC0018409. Research in the Hittinger Lab is also supported by the National Science Foundation under Grant Nos. DEB-1442148 and DEB-2110403, the United States Department of Agriculture National Institute of Food and Agriculture (Hatch Project 1020204), and the Office of the Vice Chancellor for Research and Graduate Education with funding from the Wisconsin Alumni Research Foundation (H. I. Romnes Faculty Fellow). John F. Wolters received support from National Institutes of Health (T32 HG002760-16) and National Science Foundation (Postdoctoral Research Fellowship in Biology 1907278). Ellen R. Wagner received support from the National Science Foundation Graduate Research Fellowship Program (DGE-1747503) and from the Graduate School and the Office of the Vice Chancellor for Research and Graduate Education at the University of Wisconsin-Madison with funding from the Wisconsin Alumni Research Foundation. Joshua J. Dietrich is the recipient is the recipient of a National Institutes of Health Biotechnology Training Program (NIGMS T32 GM135066).

Data availability

The mass spectrometry proteomics data have been deposited to the MassIVE database with the identifier MSV000088169. The transcriptomics data discussed in this publication has been deposited in

NCBI's Gene Expression Omnibus [59] and is accessible through GEO Series accession number GSE186126 (https://www.ncbi.nlm.nih.gov/geo/query/acc.cgi?acc=GSE186126). Intracellular metabolomics data is available on GitHub (https://github.com/AmadorNoguezLab/compartmentalized-isobutanol-pathways-in-S.-cerevisiae). The full isobutanol pathway cassette sequence containing mitochondrial-localized enzymes and flanking *HO* arms is available on GenBank with the identifier MZ541859 (Materials and methods 2.2).

Credit authorship statement

Funding acquisition: CTH, TKS, APG, DAN, YZ, BFP, JJC

Conceptualization: CTH, TKS, APG, DAN, YZ, BFP, TBJ, ERW, RLW, and FVG

Strain engineering: TKS, MT, FVG, RLW, LL, MVS

Design of experiments: FVG, TKS, BFP, CTH

Investigation: TKS, MT, FVG, JJB, JFW, TBJ, ERW, JJD, DX, JS, and SG

Data analysis: TBJ, ERW, LKM, FVG, MAM

Data visualization: FVG, ERW, LKM

Formal analysis: FVG, ERW

Writing – original draft: FVG

Writing – methods: TKS, ERW, LKM, MAM, JFW

Writing – review & editing: BFP, TKS, CTH, APG, TBJ, ERW, FVG, JJB

Declaration of competing interests

JJC is a consultant for Thermo Fisher Scientific.

Acknowledgements

We thank Kevin Myers for valuable suggestions and HyperG testing assistance, Qiang Yan for critical reading of the manuscript and Data visualization suggestions, Donna Bates & Katherine Overmyer for scheduling and suggestions, the Great Lakes Bioenergy Research Center Metabolomics Facility for metabolite quantification, and the UW-Madison Biotech center for RNA-seq.

Appendix A. Supplementary data

Supplementary data to this article can be found online at https://doi.org/10.1016/j.synbio.2022.02.007.

References

[1] Geleynse S, Brandt K, Garcia-Perez M, Wolcott M, Zhang X. The alcohol-to-jet conversion pathway for drop-in biofuels: techno-economic evaluation. ChemSusChem 2018;11:3728–41. https://doi.org/10.1002/cssc.201801690.

[2] Fu C, Li Z, Jia C, Zhang W, Zhang Y, Yi C, et al. Recent advances on bio-based isobutanol separation. Energy Convers Manag X 2021;10:100059. https://doi.org/10.1016/j.ecmx.2020.100059.

[3] Gambacorta FV, Dietrich JJ, Yan Q, Pfleger BF. Rewiring yeast metabolism to synthesize products beyond ethanol. Curr Opin Chem Biol 2020;59:182–92. https://doi.org/10.1016/j.cbpa.2020.08.005.

[4] Wess J, Brinek M, Boles E. Improving isobutanol production with the yeast *Saccharomyces cerevisiae* by successively blocking competing metabolic pathways as well as ethanol and glycerol formation. Biotechnol Biofuels 2019;12:1–15. https://doi.org/10.1186/s13068-019-1486-8.

[5] Avalos JL, Fink GR, Stephanopoulos G. Compartmentalization of metabolic pathways in yeast mitochondria improves the production of branched-chain alcohols. Nat Biotechnol 2013;31:335–41. https://doi.org/10.1038/nbt.2509.

[6] Brat D, Weber C, Lorenzen W, Bode HB, Boles E. Cytosolic re-localization and optimization of valine synthesis and catabolism enables increased isobutanol production with the yeast *Saccharomyces cerevisiae*. Biotechnol Biofuels 2012;5:1–16.

[7] Shiiba D, Miyakawa I, Sando N. Dynamic changes in mitochondrial nucleoids during the transition from anaerobic to aerobic culture in the yeast *Saccharomyces cerevisiae*. Cytologia 2005;70:287–93.

[8] Miyakawa I. Organization and dynamics of yeast mitochondrial nucleoids. Proc Japan Acad Ser B 2017;93:339–59. https://doi.org/10.2183/PJAB.93.021.

[9] Milne N, Wahl SA, van Maris AJA, Pronk JT, Daran JM. Excessive by-product formation: a key contributor to low isobutanol yields of engineered *Saccharomyces cerevisiae* strains. Metab Eng Commun 2016;3:39–51. https://doi.org/10.1016/j.meteno.2016.01.002.

[10] Bastian S, Liu X, Meyerowitz JT, Snow CD, Chen MMY, Arnold FH. Engineered ketol-acid reductoisomerase and alcohol dehydrogenase enable anaerobic 2-methylpropan-1-ol production at theoretical yield in Escherichia coli. Metab Eng 2011;13:345–52. https://doi.org/10.1016/j.ymben.2011.02.004.

[11] Matsuda F, Ishii J, Kondo T, Ida K, Tezuka H, Kondo A. Increased isobutanol production in *Saccharomyces cerevisiae* by eliminating competing pathways and resolving cofactor imbalance. Microb Cell Factories 2013;12:1–11. https://doi.org/10.1186/1475-2859-12-119.

[12] Hammer SK, Avalos JL. Uncovering the role of branched-chain amino acid transaminases in *Saccharomyces cerevisiae* isobutanol biosynthesis. Metab Eng 2017;44:302–12. https://doi.org/10.1016/j.ymben.2017.10.001.

[13] Ida K, Ishii J, Matsuda F, Kondo T, Kondo A. Eliminating the isoleucine biosynthetic pathway to reduce competitive carbon outflow during isobutanol production by *Saccharomyces cerevisiae*. Microb Cell Factories 2015;14:1–9. https://doi.org/10.1186/s12934-015-0240-6.

[14] Park S-H, Kim S, Hahn J-S. Improvement of isobutanol production in *Saccharomyces cerevisiae* by increasing mitochondrial import of pyruvate through mitochondrial pyruvate carrier. Appl Microbiol Biotechnol 2016;100:7591–8. https://doi.org/10.1007/s00253-016-7636-z.

[15] Park S-H, Hahn J-S. Development of an efficient cytosolic isobutanol production pathway in *Saccharomyces cerevisiae* by optimizing copy numbers and expression of the pathway genes based on the toxic effect of α-acetolactate. Sci Rep 2019;9:1–11. https://doi.org/10.1038/s41598-019-40631-5.

[16] Zhao EM, Zhang Y, Mehl J, Park H, Lalwani MA, Toettcher JE, et al. Optogenetic regulation of engineered cellular metabolism for microbial chemical production. Nature 2018;555:683–7. https://doi.org/10.1038/nature26141.

[17] Lane S, Zhang Y, Yun EJ, Ziolkowski L, Zhang G, Jin Y, et al. Xylose assimilation enhances production of isobutanol in engineered *Saccharomyces cerevisiae*. Biotechnol Bioeng 2019;117:1–10. https://doi.org/10.1002/bit.27202.

[18] Zhang Y, Lane S, Chen J-M, Hammer SK, Luttinger J, Yang L, et al. Xylose utilization stimulates mitochondrial production of isobutanol and 2-methyl-1-butanol in *Saccharomyces cerevisiae*. Biotechnol Biofuels 2019;12:1–15. https://doi.org/10.1186/s13068-019-1560-2.

[19] Tan SZ, Manchester S, Prather KLJ. Controlling central carbon metabolism for improved pathway yields in Saccharomyces cerevisiae. ACS Synth Biol 2016;5:116–24. https://doi.org/10.1021/acssynbio.5b00164.

[20] Feng R, Li J, Zhang A. Improving isobutanol titers in *Saccharomyces cerevisiae* with over-expressing NADPH-specific glucose-6-phosphate dehydrogenase (Zwf1). Ann Microbiol 2017;67:785–91. https://doi.org/10.1007/s13213-017-1304-0.

[21] Chen X, Nielsen KF, Borodina I, Kielland-Brandt MC, Karhumaa K. Increased isobutanol production in *Saccharomyces cerevisiae* by overexpression of genes in valine metabolism. Biotechnol Biofuels 2011;4:1–12. https://doi.org/10.1186/1754-6834-4-21.

[22] Bardone E, Bravi M, Keshavarz T, Paciello L, Parascandola P, Landi C. Auxotrophic *Saccharomyces cerevisiae* CEN.PK strains as new performers in ethanol production. Chem Eng Trans 2014;38:463–8. https://doi.org/10.3303/CET1438078.

[23] Schiestl RH, Gietz RD. High efficiency transformation of intact yeast cells using single stranded nucleic acids as a carrier. Curr Genet 1989;16:339–46. https://doi.org/10.1007/BF00340712.

[24] McIlwain SJ, Peris D, Sardi M, Moskvin OV, Zhan F, Myers KS, et al. Genome sequence and analysis of a stress-tolerant, wild-derived strain of *Saccharomyces cerevisiae* used in biofuels research. G3 Genes, Genomes, Genet 2016;6:1757–66. https://doi.org/10.1534/g3.116.029389.

[25] Liu X, Bastian S, Snow CD, Brustad EM, Saleski TE, Xu J-H, et al. Structure-guided engineering of Lactococcus lactis alcohol dehydrogenase LlAdhA for improved conversion of isobutyraldehyde to isobutanol. J Biotechnol 2012;164:188–95. https://doi.org/10.1016/j.jbiotec.2012.08.008.

[26] Christianson TW, Sikorski RS, Dante M, Shero JH, Hieter P. Multifunctional yeast high-copy-number shuttle vectors. Gene 1992;110:119–22. https://doi.org/10.1016/0378-1119(92)90454-W.

[27] Voth WP, Richards JD, Shaw JM, Stillman DJ. Yeast vectors for integration at the HO locus. Nucleic Acids Res 2001;29:e59. https://doi.org/10.1093/NAR/29.12.E59.

[28] Gueldener U, Heinisch J, Koehler GJ, Voss D, Hegemann JH. A second set of loxP marker cassettes for Cre-mediated multiple gene knockouts in budding yeast. Nucleic Acids Res 2002;30:e23. https://doi.org/10.1093/nar/30.6.e23.

[29] Stoneman HR, Wrobel RL, Place M, Graham M, Krause DJ, Chiara M De, et al. CRISpy-pop: a web tool for designing CRISPR/Cas9-driven genetic modifications in diverse populations. G3 Genes, Genomes, Genet 2020;10:4287–94. https://doi.org/10.1534/G3.120.401498.

[30] Higgins DA, Young MKM, Tremaine M, Sardi M, Fletcher JM, Agnew M, et al. Natural variation in the multidrug efflux pump SGE1 underlies ionic liquid tolerance in yeast. Genetics 2018;210:219–34. https://doi.org/10.1534/genetics.118.301161.

[31] Ghosh IN, Martien J, Hebert AS, Zhang Y, Coon JJ, Amador-Noguez D, et al. OptSSeq explores enzyme expression and function landscapes to maximize isobutanol production rate. Metab Eng 2018;52:324–40. https://doi.org/10.1016/J.YMBEN.2018.12.008.

[32] Güldener U, Heck S, Fielder T, Beinhauer J, Hegemann JH. A new efficient gene disruption cassette for repeated use in budding yeast. Nucleic Acids Res 1996;24:2519–24. https://doi.org/10.1093/NAR/24.13.2519.

[33] Jacobson TB, Korosh TK, Stevenson DM, Foster C, Maranas C, Olson DG, et al. In vivo thermodynamic analysis of glycolysis in Clostridium thermocellum and thermoanaerobacterium saccharolyticum using 13 C and 2 H tracers. mSystems 2020;5. https://doi.org/10.1128/mSystems.00736-19. e00736-19.
[34] Jacobson TB, Adamczyk PA, Stevenson DM, Regner M, Ralph J, Reed JL, et al. 2 H and 13 C metabolic flux analysis elucidates in vivo thermodynamics of the ED pathway in Zymomonas mobilis. Metab Eng 2019;54:301–16. https://doi.org/10.1016/j.ymben.2019.05.006.
[35] Melamud E, Vastag L, Rabinowitz JD. Metabolomic analysis and visualization engine for LC−MS data. Anal Chem 2010;82:9818–26. https://doi.org/10.1021/AC1021166.
[36] Clasquin MF, Melamud E, Rabinowitz JD. LC-MS data processing with MAVEN: a metabolomic analysis and visualization engine. Curr Protoc Bioinf. 2012;37. https://doi.org/10.1002/0471250953.BI1411S37. 14–11.
[37] Gasch AP. Yeast genomic expression studies using DNA microarrays, vol. 350. Academic Press; 2002. https://doi.org/10.1016/S0076-6879(02)50976-9.
[38] Bolger AM, Lohse M, Usadel B. Trimmomatic: a flexible trimmer for Illumina sequence data. Bioinformatics 2014;30:2114–20. https://doi.org/10.1093/BIOINFORMATICS/BTU170.
[39] Langmead B. Aligning short sequencing reads with Bowtie, vol. 11; 2010. https://doi.org/10.1002/0471250953.bi1107s32.
[40] Anders S, Pyl PT, Huber W. HTSeq—a Python framework to work with high-throughput sequencing data. Bioinformatics 2015;31:166–9. https://doi.org/10.1093/BIOINFORMATICS/BTU638.
[41] Robinson MD, McCarthy DJ, Smyth GK. edgeR: a Bioconductor package for differential expression analysis of digital gene expression data. Bioinformatics 2010;26:139–40. https://doi.org/10.1093/bioinformatics/btp616.
[42] Benjamini Y, Hochberg Y. Controlling the false discovery rate: a practical and powerful approach to multiple testing. J Roy Stat Soc 1995;57:289–300.
[43] de Hoon MJL, Imoto S, Nolan J, Miyano S. Open source clustering software. Bioinformatics 2004;20:1453–4. https://doi.org/10.1093/BIOINFORMATICS/BTH078.
[44] Saldanha AJ. Java Treeview—extensible visualization of microarray data. Bioinformatics 2004;20:3246–8. https://doi.org/10.1093/BIOINFORMATICS/BTH349.
[45] Simillion C, Liechti R, Lischer HEL, Ioannidis V, Bruggmann R. Avoiding the pitfalls of gene set enrichment analysis with SetRank. BMC Bioinf 2017;18:1–14. https://doi.org/10.1186/S12859-017-1571-6.
[46] Shishkova E, Hebert AS, Westphall MS, Coon JJ. Ultra-high pressure (>30,000 psi) packing of capillary columns enhancing depth of shotgun proteomic analyses. Anal Chem 2018;90:11503–8. https://doi.org/10.1021/ACS.ANALCHEM.8B02766.
[47] Cox J, Mann M. MaxQuant enables high peptide identification rates, individualized p.p.b.-range mass accuracies and proteome-wide protein quantification. Nat Biotechnol 2008;26:1367–72. https://doi.org/10.1038/nbt.1511.
[48] Robinson MD, Grigull J, Mohammad N, Hughes TR. FunSpec: a web-based cluster interpreter for yeast. BMC Bioinf 2002;3:1–5. https://doi.org/10.1186/1471-2105-3-35.
[49] Lazar DN, Brem RB, Kruglyak L, Gottschling DE. Polymorphisms in multiple genes contribute to the spontaneous mitochondrial genome instability of *Saccharomyces cerevisiae* S288C strains. Genetics 2009;183:365–83. https://doi.org/10.1534/GENETICS.109.104497.
[50] Fred S. Getting started with yeast. Methods Enzymol 2002;350:3–41.
[51] Lee ME, DeLoache WC, Cervantes B, Dueber JE. A highly characterized yeast toolkit for modular, multipart assembly. ACS Synth Biol 2015;4:975–86. https://doi.org/10.1021/sb500366v.
[52] Sun J, Shao Z, Zhao H, Nair N, Wen F, Xu J-H, et al. Cloning and characterization of a panel of constitutive promoters for applications in pathway engineering in *Saccharomyces cerevisiae*. Biotechnol Bioeng 2012;109:2082–92. https://doi.org/10.1002/bit.24481.
[53] Martínez-Pastor MT, Perea-García A, Puig S. Mechanisms of iron sensing and regulation in the yeast S*accharomyces cerevisiae*. World J Microbiol Biotechnol 2017;33:1–9. https://doi.org/10.1007/s11274-017-2215-8.
[54] Ljungdahl PO, Daignan-Fornier B. Regulation of amino acid, nucleotide, and phosphate metabolism in *Saccharomyces cerevisiae*, vol. 190. Oxford Academic; 2012. https://doi.org/10.1534/GENETICS.111.133306.
[55] Bamba T, Yukawa T, Guirimand G, Inokuma K, Sasaki K, Hasunuma T, et al. Production of 1,2,4-butanetriol from xylose by *Saccharomyces cerevisiae* through Fe metabolic engineering. Metab Eng 2019;56:17–27. https://doi.org/10.1016/j.ymben.2019.08.012.
[56] Salusjärvi L, Toivari M, Vehkomäki M-L, Koivistoinen O, Mojzita D, Niemelä K, et al. Production of ethylene glycol or glycolic acid from D-xylose in *Saccharomyces cerevisiae*. Appl Microbiol Biotechnol 2017;101:8151–63. https://doi.org/10.1007/s00253-017-8547-3.
[57] Yamaguchi-Iwai Y, Dancis A, Klausner RD. AFT1: a mediator of iron regulated transcriptional control in *Saccharomyces cerevisiae*. EMBO J 1995;14:1231–9. https://doi.org/10.1002/j.1460-2075.1995.tb07106.x.
[58] Benisch F, Boles E. The bacterial Entner-Doudoroff pathway does not replace glycolysis in Saccharomyces cerevisiae due to the lack of activity of iron-sulfur cluster enzyme 6-phosphogluconate dehydratase. J Biotechnol 2014;171:45–55. https://doi.org/10.1016/j.jbiotec.2013.11.025.
[59] Edgar R, Domrachev M, Lash AE. Gene Expression Omnibus: NCBI gene expression and hybridization array data repository. Nucleic Acids Res 2002;30:207–10. https://doi.org/10.1093/NAR/30.1.207.